

Natural Garnet Reference Materials for the Electron Microprobe Flank Method to Determine the $\text{Fe}^{3+}/\Sigma\text{Fe}$ of Unknown Garnets

Wen-Tan Xu,^a Di-Cheng Zhu,^{b, c,*} Qing Wang,^a Liang-Liang Zhang,^b Jin-Cheng Xie,^b Ze Liu,^a and Si-Hua Yuan^d

^a State Key Laboratory of Geological Processes and Mineral Resources, School of Earth Sciences and Resources, China University of Geosciences, Beijing 100083, P. R. China

^b State Key Laboratory of Geological Processes and Mineral Resources, and Institute of Earth Sciences, China University of Geosciences, Beijing 100083, P. R. China

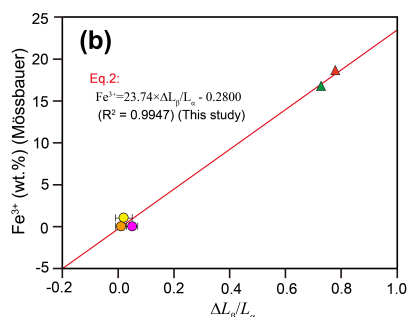
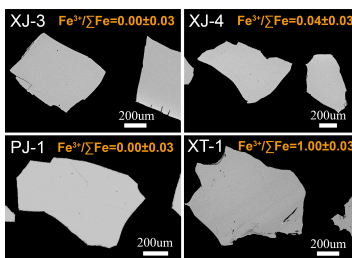
^c Frontiers Science Center for Deep time Digital Earth, China University of Geosciences, Beijing 100083, P. R. China

^d School of Earth sciences and Engineering, University of Emergency Management, Langfang 065201, P. R. China

Received: February 26, 2026; Revised: March 30, 2026; Accepted: March 31, 2026; Available online: April 11, 2026.

DOI: 10.46770/AS.2026.028

ABSTRACT: The oxidation state of minerals enriched in ferrous or ferric irons is a direct proxy for magma oxygen fugacity. The electron probe microanalysis (EPMA) flank method is highly efficient and easily accessible in the determination of oxidation state of Fe-rich minerals. The determination of $\text{Fe } L_{\alpha}$ and $\text{Fe } L_{\beta}$ at flank positions is crucial to calibrate Fe oxidation state of garnets using EPMA flank method, which relies on pure Fe^{2+} and Fe^{3+} end-number garnets as references. However, the practical application of this method is restricted by the scarcity of natural reference materials. To address this limitation, this study investigates several natural garnets to evaluate their potential as reference materials for the EPMA flank method. EPMA major element analysis and mapping results revealed that samples XJ-3 and PJ-1 are compositionally homogeneous and can be classified as almandine. In contrast, sample XT-1, identified as andradite, exhibits compositional zoning. Mössbauer spectroscopy analysis further confirmed the iron valence states of these garnets: the $\text{Fe}^{3+}/\Sigma\text{Fe}$ ratios of almandine samples XJ-3, PJ-1, and XJ-4 are 0.00 ± 0.03 , 0.00 ± 0.03 , and 0.04 ± 0.03 , respectively, while the andradite sample XT-1 shows a $\text{Fe}^{3+}/\Sigma\text{Fe}$ ratio of 1.00 ± 0.03 . These results demonstrate that XJ-3, PJ-1 (as Fe^{2+} -dominant end-members) and XT-1 (as Fe^{3+} -dominant end-member) are suitable for determining the flank positions of $\text{Fe } L_{\alpha}$ and $\text{Fe } L_{\beta}$. This study further quantified the relationship between the $\text{Fe } L_{\alpha}/L_{\beta}$ intensity ratio at the calibrated flank positions and the Fe^{2+} or Fe^{3+} content of garnets. A simple linear regression equation was established, and the method based on this equation yields an uncertainty of ± 1 wt% for Fe^{2+} content and ± 0.05 for the $\text{Fe}^{3+}/\Sigma\text{Fe}$ ratio. In conclusion, the natural garnet samples of XJ-3, PJ-1, and XT-1 investigated in this study can serve as reliable reference materials for the EPMA flank method, enabling accurate determination of the Fe oxidation state in unknown garnet samples.



INTRODUCTION

Oxygen fugacity, a critically geochemical parameter characterizing magmatic conditions, exerts a profound influence on magmatic processes and mineralization,^{1,2} which achieves this by altering the solubility of valence-variable elements,^{3,4}

modifying the properties of subduction zone fluids,^{5,6} and changing mineral stability.^{7,8} During magmatic evolution, the accumulation and fractional crystallization of minerals enriched in Fe^{2+} (i.e., with low $\text{Fe}^{3+}/\Sigma\text{Fe}$ ratios), such as garnet, amphibole, and phlogopite, result in increasing oxidation of the residual melt.⁹⁻¹¹ Accurate determination of the Fe oxidation state in Fe-rich

minerals is therefore a key prerequisite for unraveling variations in oxygen fugacity during magmatic and mineralization processes.^{2,12} Wet chemistry and Mössbauer spectroscopy are two conventional methods for quantifying Fe³⁺/ΣFe ratios in minerals. However, these techniques typically require powdered samples. Furthermore, the presence of mineral inclusions may induce significant deviations in experimental results. *In-situ* analytical techniques, including X-ray absorption near-edge structure (XANES) spectroscopy, electron energy loss spectroscopy (EELS), and X-ray photoelectron spectroscopy (XPS), have been employed for determining the Fe oxidation state in geological samples.^{13–17} Nevertheless, these techniques suffer from inherent limitations: for instance, XANES relies on a synchrotron X-ray source, while EELS and XPS are prone to beam damage, constraining their widespread application for Fe³⁺/ΣFe determination in Fe-rich minerals. Notably, EPMA flank method is a highly promising alternative. First applied by Höfer et al. (1994)¹⁸ to determine Fe³⁺/ΣFe ratios in iron oxides, the EPMA flank method has gained broader utility owing to its accessibility and efficiency. It has since been successfully applied to calcic pyroxene,^{19–21} amphibole,^{22–24} biotite,²⁴ garnet,^{10,25–28} and silicate glass.^{29,30}

The EPMA flank method relies on the peak shifts and energy differences of the Fe *L*_α and Fe *L*_β emission lines, which arise from the self-absorption effects of Fe²⁺ and Fe³⁺.^{18,24} A core procedure of this method is to determine the flank positions of Fe *L*_α and Fe *L*_β using reference garnets of pure Fe²⁺ end-member (almandine) and Fe³⁺ end-member (andradite). This is because Fe²⁺ content exhibits a linear correlation with the Fe *L*_α/Fe *L*_β intensity ratio at the calibrated flank positions. For garnets with a total Fe content of 10 wt%, the EPMA flank method has a reported accuracy of ± 0.04 for the Fe³⁺/ΣFe ratio.²⁵ Previous studies have typically employed synthetic end-member garnets for EPMA flank measurements.²⁵ Owing to the difference of ionic radius, synthetic end-member garnets always show potential lattice defects. In addition, complicated synthesis techniques and potential

compositional inhomogeneity further hinder the application of EPMA flank method. In contrast to synthetic garnet materials, natural garnets are easily obtained and have similar matrix effect to testing samples, leading to an ideal choice for EPMA flank method. However, the availability of natural garnet standards is severely limited, hindering their broader application in this method.

In this study, a suite of natural garnet grains was collected to identify potential reference materials for the EPMA flank method. EPMA major element analysis and elemental mapping were used to assess compositional homogeneity and chemical end-member characteristics, while Mössbauer spectroscopy was employed to quantify Fe³⁺/ΣFe ratios. Our results indicate that XJ-3, PJ-1, and XT-1 are suitable natural reference materials, and they can be used not only to determine the critical flank positions but also to calibrate the Fe³⁺/ΣFe ratio of unknown garnet samples.

EXPERIMENTAL

Sample description and preparation. A total of eight garnet samples were collected from Pakistan and China, consisting of both gem-quality crystals or small grains. These sample were first roughly crushed to 30–50 mesh, followed by careful examination under a binocular microscope to select inclusion-free garnet fragments. The examination results indicate that XJ-3, XJ-4 and XT-2 contain inclusions. These inclusion-bearing samples further crushed to 80 mesh, and are carefully examined under a binocular microscope to select inclusion-free garnet fragments. The step-by-step crushing and precise examination garnet fragments can ensure that these garnet fragments do not contain inclusions. Approximately 30 fragments per sample were embedded in epoxy resin and polished using diamond paste to obtain mirror-like surfaces. Backscattered electron (BSE) imaging was subsequently employed to assess compositional zoning within the garnet grains (Fig. 1).

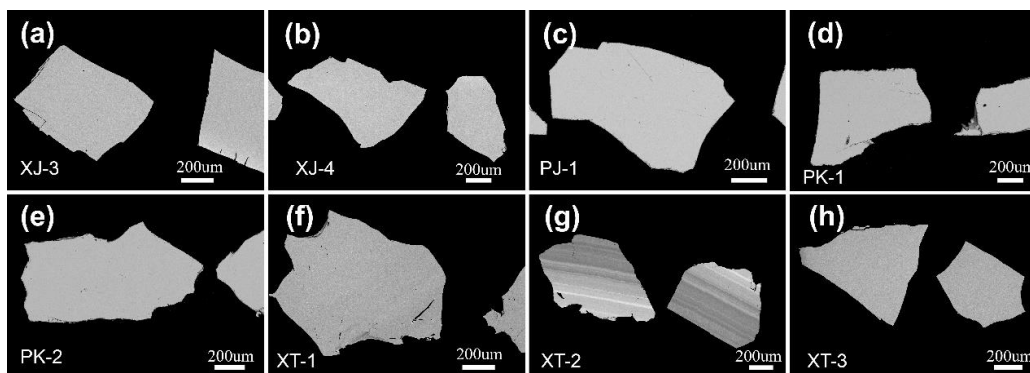


Fig. 2 Backscattered electron images of selected garnet fragments. (a–b) almandite from Koktokay, Xinjiang Uygur Autonomous Region and (c) almandite from Pingjiang county, Hunan Province and (d–e) grossular from gilgit Baltistan, Pakistan and (f–g) andradite from Khyber Pakhtunkhwa Province, Pakistan and (h) from Hebei Province.

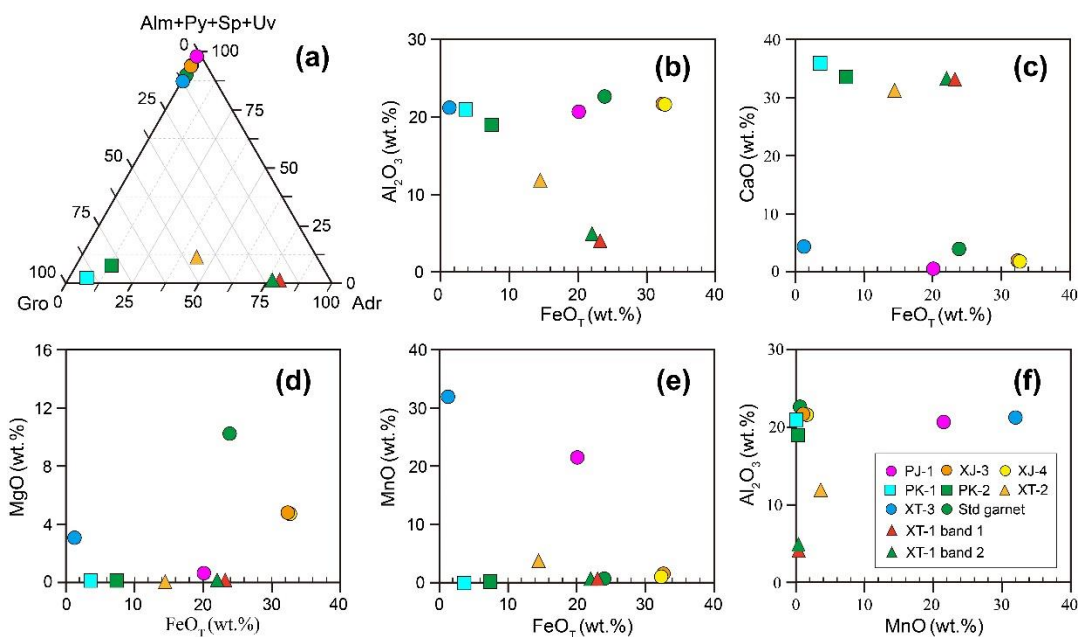


Fig. 3 Garnet end-members (a) and chemical compositions of selected samples (b-f).

EPMA analysis of major elements. Major element analyses were performed using a JEOL JXA-8230 electron probe microanalyzer (EPMA) equipped with four wavelength-dispersive spectrometers (WDS) at the Hebei Key Laboratory of Earthquake Dynamics (HKLED), University of Emergency Management, China. Consistent analytical conditions were employed for all elements: accelerating voltage of 15 kV, beam current of 20 nA, and beam diameter of 5 μm . Peak counting times and background counting times (upper and lower backgrounds) were optimized for different elements: 20 s (peak) and 10 s (background) for Si, Al, Fe, Mg, and Ca; 40 s (peak) and 20 s (background) for Mn, Cr, Ni, and Ti; and 10 s (peak) and 5 s (background) for Na and K. Calibration was conducted using the following reference standards: chromediopside (for Si and Ca), almandine (Al), jadeite (Na), olivine (Mg), orthoclase (K), rutile (Ti), magnetite (Fe), bustamite (Mn), chromium oxide (Cr_2O_3 , for Cr), and pentlandite (Ni). Analytical accuracy was verified: major element contents deviated by $\leq \pm 2\%$ from preferred values, while minor element contents showed deviations within 10% of preferred values. All elemental data were processed with ZAF correction (atomic number, absorption, and fluorescence corrections) using proprietary Shimadzu software.

EPMA mapping analysis. To evaluate the compositional homogeneity of the studied garnet samples, major elemental distribution mapping was performed using a JEOL JXA-8230 electron probe microanalyzer (EPMA) located at the HKLED, University of Emergency Management, China. The analyses were conducted under the following optimized conditions: accelerating voltage of 15 kV, beam current of 50 nA, and an electron beam defocused to a 1 μm diameter. For high-resolution mapping results,

a pixel size of 1 $\mu\text{m} \times 1 \mu\text{m}$ was adopted, consistent with the defocused beam diameter. The dwell time per pixel was set to 200 ms to ensure sufficient signal-to-noise ratio for accurate elemental distribution characterization.

Mössbauer analysis of the $\text{Fe}^{3+}/\Sigma\text{Fe}$ ratio. $\text{Fe}^{3+}/\Sigma\text{Fe}$ ratios of the selected garnet samples were determined using Mössbauer spectroscopy. The crushed garnet fragments were cleaned in an ultrasonic bath with ethanol, followed by Milli-Q water, for 5 minutes each to remove surface impurities. The garnet fragments were then ground to 200 mesh powder using an agate mortar before Mössbauer analyses. All samples were analyzed using a WSS-10 Mössbauer spectrometer at Guangzhou Institute of Geochemistry, Chinese Academy of Sciences. A ^{57}Co source with an activity of 25 mCi in a rhodium matrix was employed during all analyses. Mössbauer spectra of the garnet powder were collected using a moving absorber at room temperature. A standard absorber, $\alpha\text{-Fe}$ foil with a thickness of 25 μm , was used to calibrate the velocity scale. MossWinn 4.0 software was utilized to analyze the Mössbauer spectra, which were fitted using a Lorentzian linear distribution through the least squares method. The quality of the fits to the Mössbauer spectra of the samples indicates that the 1σ uncertainty of $\text{Fe}^{3+}/\Sigma\text{Fe}$ ranges from 0.01 to 0.05.

RESULTS AND DISCUSSION

Major element composition of garnet. Eight garnet samples were selected for EPMA major element analysis. To monitor the

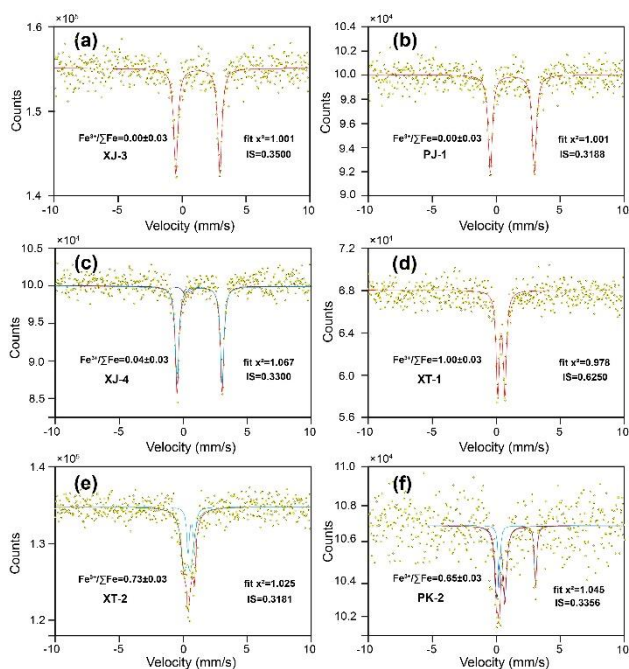


Fig. 3 Mössbauer spectra of the garnet samples.

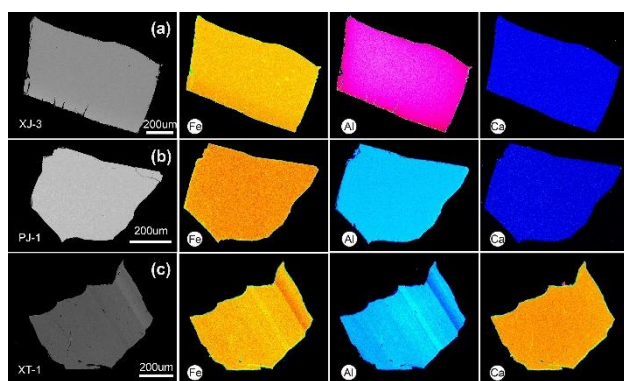


Fig. 4 Backscattered electron images and mapping results.

accuracy of the EPMA analytical conditions, one standard garnet sample was additionally analyzed. The raw analytical results are summarized in Table S1, while the mean major element compositions of all nine samples are listed in Table S2. Samples PJ-1, XJ-3, XJ-4, and XT-3 belong to the almandine–pyrope–grossular (Alm-Py-Gro) series (Fig. 2a) and show variable contents of FeO, MgO, and MnO (Fig. 2b–2f). Samples PK-1 and PK-2 belong to the grossular (Gro) series, distinguished by high Al_2O_3 (18.97–20.96 wt%) and CaO (33.54–35.91 wt%) contents, as well as low total FeO (TFeO; 3.60–7.39 wt%) (Fig. 2a–2c). Samples XT-1 and XT-2 are identified as andradite (Adr) end-members, featuring relatively high CaO and TFeO contents coupled with low Al_2O_3 (Fig. 2a–2c).

$\text{Fe}^{3+}/\Sigma\text{Fe}$ ratio of garnet obtained by Mössbauer spectroscopy.

Mössbauer spectroscopy results are presented in Fig. 3. The spectra results indicate that samples XJ-3 and PJ-1 contain pure ferrous iron (Fe^{2+}), with a $\text{Fe}^{2+}/\Sigma\text{Fe}$ ratio of 1.00 ± 0.03 for both. Sample XJ-4 is also enriched in Fe^{2+} , exhibiting a low $\text{Fe}^{3+}/\Sigma\text{Fe}$ ratio of 0.04 ± 0.03 . In contrast, the grossular (Gro) series samples XT-1 and XT-2 are enriched in ferric iron (Fe^{3+}). XT-1 has a $\text{Fe}^{3+}/\Sigma\text{Fe}$ ratio of 1.00 ± 0.03 , while XT-2 shows a $\text{Fe}^{3+}/\Sigma\text{Fe}$ ratio of 0.73 ± 0.03 . Additionally, the low TFeO PK-2 sample yielded $\text{Fe}^{3+}/\Sigma\text{Fe}$ ratios of 0.65 ± 0.03 .

Selection of standard samples.

The key to calculating the $\text{Fe}^{2+}/\Sigma\text{Fe}$ ratio of garnets lies in determining the flank positions of $\text{Fe } L_\alpha$ and $\text{Fe } L_\beta$ emission lines, which are defined using pure Fe^{2+} end-member (almandine) and Fe^{3+} end-member (andradite) reference materials. The principle of garnet reference materials selection using to determine Fe flank method positions are homogeneity, inclusion-free, pure Fe^{2+} and Fe^{3+} end-member, and relatively high TFeO. PK-1 and PK-2 are grossular with TFeO contents less than 10 wt% (Fig. 2b–2c). Although, XT-3 belongs to Alm-Py-Sp-Uv series, it has high MnO and significantly low TFeO and belongs to spessartine. Previous study suggested that the flank method can yield an accuracy of $\text{Fe}^{3+}/\Sigma\text{Fe}$ at ± 0.04 for garnets with the total Fe content more than 10wt%.³¹ Therefore, garnets with TFeO contents less than 10 wt% can yield larger accuracy. XT-2 is andradite with relatively high TFeO. However, this sample has complex compositionally zoning with $\text{Fe}^{3+}/\Sigma\text{Fe}$ ratio of 0.73 ± 0.03 , leading to a complexity between Fe content and Fe valence. Therefore, only XJ-3, PJ-1, and XT-1 were discussed in the subsequent research.

As demonstrated earlier, samples XJ-3 and PJ-1 qualify as natural pure Fe^{2+} end-members, with a $\text{Fe}^{2+}/\Sigma\text{Fe}$ ratio of 1.00 ± 0.03 for both. To further verify the compositional homogeneity of these two samples, EPMA elemental mapping analyses were conducted. The mapping results confirm that both garnet samples are compositionally homogeneous (Fig. 4a and 4b). Sample XT-1 is a potential pure Fe^{3+} end-member (andradite). Nevertheless, its backscattered electron (BSE) image reveals alternating dark and bright compositional bands (Fig. 4c and 5a). A linear compositional profile across one XT-1 garnet grain exhibits an inverse correlation between total FeO and Al_2O_3 contents (Fig. 5b), which is consistent with the elemental mapping results (Fig. 4c). Based on the molar proportions of garnet end-members calculated following Locock (2008),³² XT-1 is predominantly composed of 74–80% andradite and 17–25% grossular, with almost no almandine component (Fig. 5c). Additionally, a clear negative correlation is observed between octahedral Fe^{3+} , Al, and Mn atoms per formula unit (Fig. 5d). Combined with the Mössbauer spectroscopy results ($\text{Fe}^{3+}/\Sigma\text{Fe} = 1.00 \pm 0.03$), we suggest that XT-1 qualifies as a pure Fe^{3+} end-member. It can be used together with XJ-3 and PJ-1 (pure Fe^{2+} end-members) to define the flank positions of $\text{Fe } L_\alpha$ and $\text{Fe } L_\beta$ emission lines.

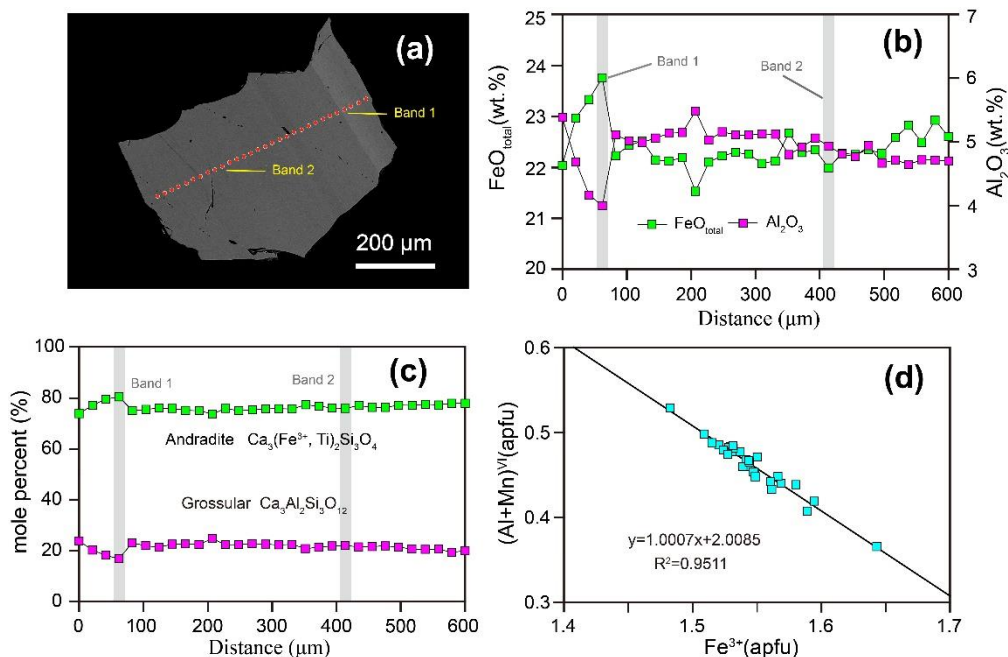


Fig. 5 Compositional profile across the XT-1 fragment (a) backscattered electron image showing chemically compositional bands and test positions (white circles) (b) variations of total FeO and Al₂O₃ contents and (c) calculated mole percentage (%) of andradite and grossular end-members across the XT-1 fragment and (d) Fe³⁺ versus (Al+Mn)^{VI} atoms per formula unit (apfu) calculated on the basis of 8 cations per 12 oxygens.

Spectrometer calibration before EMPA flank method analysis.

The accuracy of the EPMA flank method is strongly governed by the long-term stability of the TAP crystal in the JEOL JXA-8230 electron probe microanalyzer. This stability is influenced by laboratory environmental factors, including electromagnetic interference, temperature, humidity, and air pressure, which may induce shifts in spectral positions. Therefore, daily spectrometer calibration is a prerequisite for conducting flank method analyses.²⁵ Two calibration procedures have been proposed to correct the mentioned spectrometer position offsets.^{25,28} Prior to calibration, the detector slit of the TAP spectrometer was adjusted to 300 μm to obtain sharp peaks. Firstly, the calibration procedure proposed by Höfer and Brey (2007)²⁵ was implemented. Specifically, we used a Fe metal standard to search the FeKα₁ 9th order peak with the operation conditions of 25 kV, 80 nA, and a 1 μm beam in TAP crystal. The FeKα₁ 9th order peak (fe₀) is 189.300 nm. Subsequently, we performed a 50 μm interval on both sides (fe₁ and fe₂) of fe₀ peak to measure the counts of these two positions. And then measured counts from four positions shifted by ±5 μm from fe₁ and fe₂ positions. The above six positions were measured with a duration of 180 seconds, and repeated three times. The measured results were plotted against the regression line to determine the offset values. The above procedure always takes 1 hour in our laboratory. On the next day, we performed a spectrometer initialization (SPI) procedure with the operation conditions of 20 kV, 20 nA, using a metal Mg as the internal standard.²⁸ The overall SPI procedure always takes 20 min. After

the spectrometer initialization, we repeated the spectrometer calibration procedure performed in the first day. And we also conducted a 14 μm spectrometer calibration procedure after SPI to compare the influence of offset distance.²⁶

Höfer and Brey (2007)²⁵ noted that a fe₁/fe₂ ratio of 1 indicates peak symmetry in the measured region. Otherwise, correction of the spectrometer position is necessary. Our results showed that fe₁/fe₂ ratios before SPI ranged from 0.858 to 0.866, indicating a relatively large spectral shift. In contrast, fe₁/fe₂ ratios after SPI ranged from 0.977 to 1.02, which are close to the "true" peak position (Fig. 6a). The 14 μm offset calibration yielded fe₁/fe₂ ratios of 0.985 to 1.013, which were similar with those obtained with the 50 μm offset (Fig. 6b). This result suggests that long-distance offsets do not significantly affect the spectrometer position correction efficiency. Therefore, the SPI procedure can be implemented as a daily routine to correct spectrometer positional shifts for EPMA flank method analyses.

Identifying the flank position of Fe L_α and Fe L_β. Owing to the difference in self-absorption between Fe²⁺ and Fe³⁺, the ferrous iron (Fe²⁺) content exhibits a systematic correlation with the intensities of Fe L_α and Fe L_β emission lines at their flank positions.²⁵ These flank positions of Fe L_α and Fe L_β can be determined using pure Fe²⁺ end-member (almandine) and Fe³⁺ end-member (andradite) garnets. Sample XJ-3 was selected as the pure Fe²⁺ end-member garnet because its TFeO content (32.46 wt%)

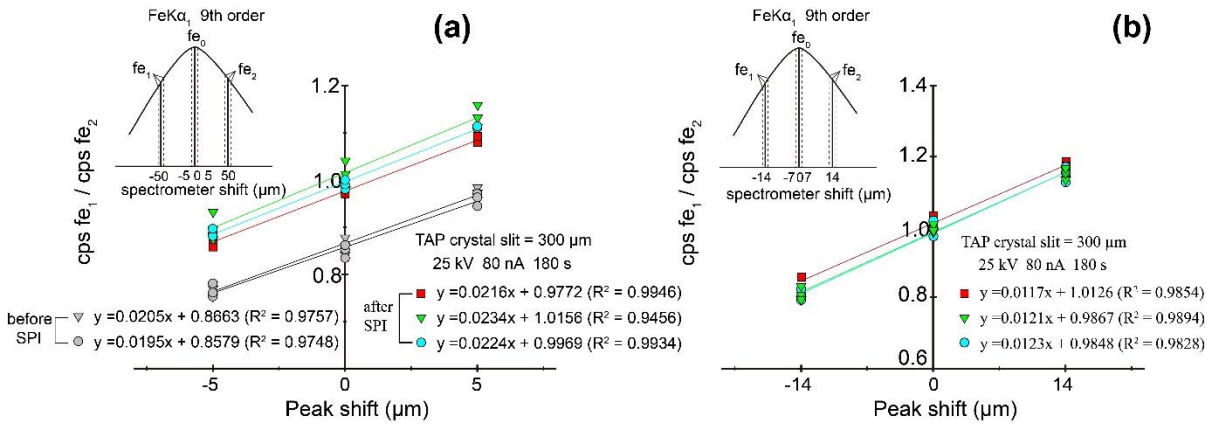


Fig. 6 Comparison of the spectrometer position before and after the operation of spectrometer initialization (a) a 50 μm spectrometer shift before and after spectrometer initialization and (b) a 14 μm spectrometer shift after spectrometer initialization.

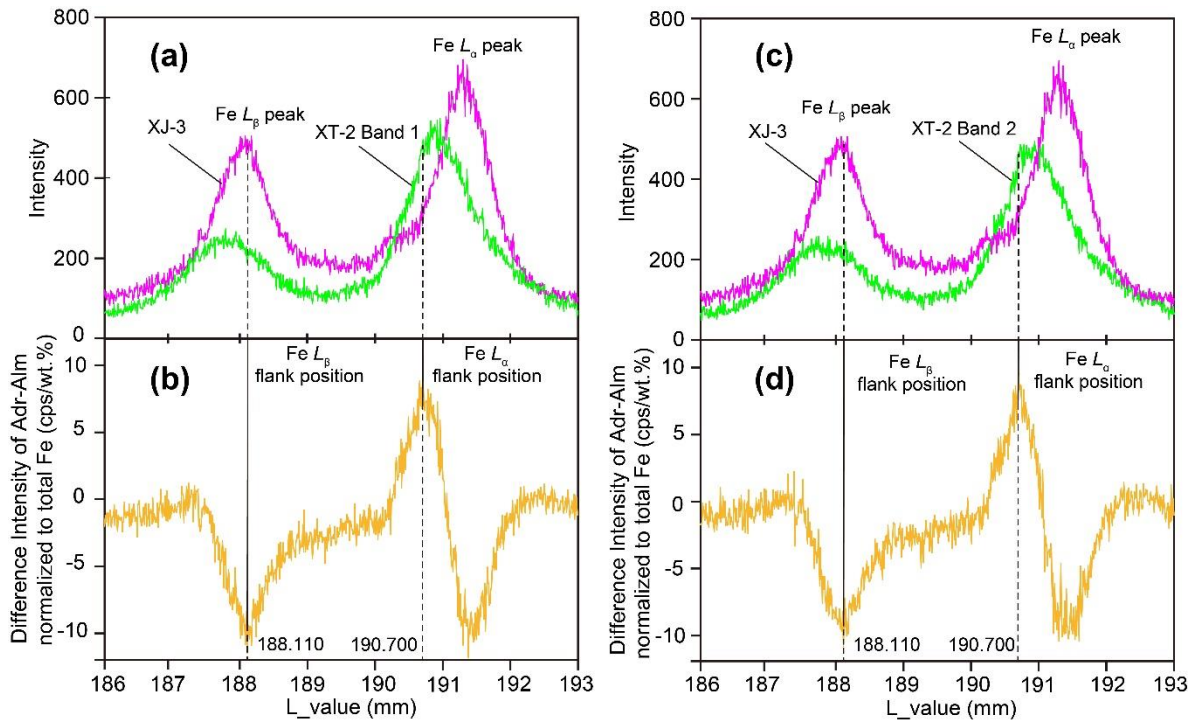


Fig. 7 Determination of Fe L_α and Fe L_β flank positions based on andradite and almandine reference samples (a and c) raw spectra of the Fe L-line of XJ-3 with XT-2 band1 and band 2, which were collected at 15 kV, 80 nA, and 10 μm probe diameter and (b and d) difference spectra between XJ-3 with XT-2 band1 and band 2, which were normalized by using their Fe content, respectively. The flank positions of Fe L_α and L_β were located using the maximum and minimum intensities on the difference spectrums.

is relatively higher than that of PJ-1 (20.08 wt%). To evaluate the potential influence of chemical composition variations on the determination of Fe L_α and Fe L_β flank positions, wavelength scans were performed on two bands (Band 1 and Band 2) of the pure Fe³⁺ end-member garnet XT-1, which have different TFeO contents (Fig. 5b). We used an accelerating voltage of 15 kV, 80 nA probe current, and a beam current of 10 μm operation conditions to conducted the wave scan with the L value for TAP

spectrometer ranging from 186 to 193 mm. The wavelength scan results are presented in Fig. 7. The results show a tendency of Fe L_α and L_β of XT-1 shifted to higher wavelength compared to andradite samples due to self-absorption (Fig. 7a and 7c). We defined the maximum and minimum values of the intensity difference between Fe L_α and Fe L_β as the L_α flank position and L_β flank position, respectively (Fig. 7b and 7d). XT-1 band 1 and band 2 exhibit identical Fe L_α and Fe L_β flank positions, suggesting that

chemical composition differences do not affect the determination of flank positions. The flank method for the determination of Fe L_α and L_β is related to the $L_{2,3}$ absorption.³³ The similarity between $L_{2,3}$ -edge absorption energy and the L line emission energy trigger an X-ray resonant process involving both X-ray absorption and X-ray emission. L_α in flank position is close to L_{3} -edge absorption, whose absorption coefficient is significantly larger than L_β . L_β in flank position is far from L_{2} -edge absorption, and is nearly keep a certain position.³⁴ Thus, the intensity of L_α in flank position is related to the Fe^{2+} contents, and independent of Fe^{3+} content. Therefore, chemical compositional differences may not affect the determination of flank positions.

Considering the high TFeO content of XT-1 Band 1, XJ-3 (pure Fe^{2+} end-member) and XT-1 Band 1 (pure Fe^{3+} end-member) were used to determine the target flank positions. The Fe L_α and Fe L_β flank positions obtained in this study (190.700 mm and 188.110 mm, respectively) are nearly identical to the theoretical flank positions (190.720 mm and 188.095 mm, respectively).

Analyses of Fe L_α and Fe L_β at flank positions. In this study, the Fe L_α and Fe L_β flank positions determined using XJ-3 and XT-1 Band 1 were employed to acquire the spectral intensities at these two positions. The analyses were conducted under operating conditions of 15 kV accelerating voltage, 60 nA beam current, and 5 μm beam diameter. To improve counting statistics, 16 flank method analyses per sample were performed.³² We added two “fake” elements of As and Br at one TAP spectrometer to represent the Fe L_α and L_β flank positions, respectively. A counting time of 180 s was applied at each of these two flank positions to ensure sufficiently high counts. To verify the reliability of the flank method in our laboratory, a set of standard garnet samples (AND1, FRA1, Damknolle, Mir1, Mir2, Mir13, Mir23, and UA5) with known $\text{Fe}^{3+}/\Sigma\text{Fe}$ ratios were also analyzed.^{27,28} The EPMA major element compositions and Fe L_β/L_α intensity ratios at the flank positions of these eight standard garnet samples are provided in Table S5.

The Fe L_β/L_α intensity ratios measured by EPMA at the flank positions exhibit a strong positive correlation with the Fe^{2+} contents of the standard garnets (Fig. 8). Based on this correlation, a linear regression equation was established for the standard garnet samples: $L_\beta/L_\alpha = 0.0400 \times \text{Fe}^{2+} + 0.5811$ ($R^2 = 0.9899$). This equation is highly consistent with those reported by previous study.^{27,28}

Therefore, the flank method established in this study is applicable for determining the Fe oxidation state of unknown garnet samples, and XJ-3 and XT-1 are reliable reference materials for defining the Fe L_α and Fe L_β flank positions.

Calculation of garnet Fe^{2+} content and the $\text{Fe}^{3+}/\Sigma\text{Fe}$ ratio. Using the validated analytical parameters described above, we measured the spectral intensities at the Fe L_α and Fe L_β flank positions

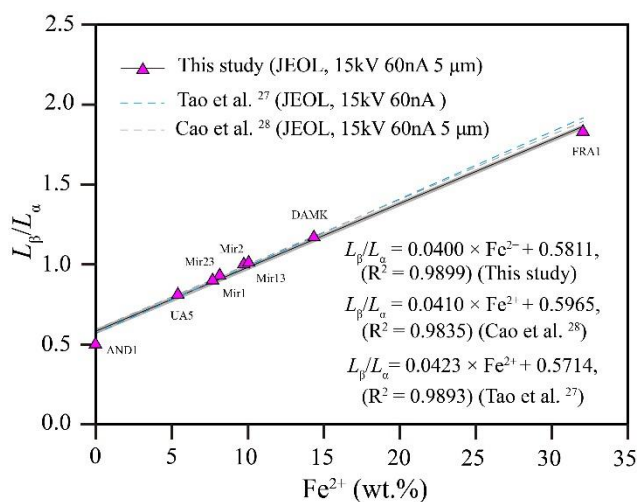


Fig. 8 Simple linear regression of Fe L_β/L_α intensity ratios (flank position ratios) against Fe^{2+} contents for reference standard garnets. (The simple linear regression of blue dotted line and grey dotted line for these standard garnets are from Tao et al.²⁷ and Cao et al.²⁸).

for the garnet samples whose Fe^{2+} contents were calculated from the total FeO and Mössbauer $\text{Fe}^{3+}/\Sigma\text{Fe}$ ratios, ranging from 0 to 25.23 wt.%. The plot of L_β/L_α ratio against the Fe^{2+} contents of samples determined by Mössbauer is shown in Fig. 9a. A simple linear regression analysis yields an equation:

$$L_\beta/L_\alpha = 0.0431 \times \text{Fe}^{2+} + 0.5014 \quad (R^2 = 0.9977) \quad (1)$$

Based on linear regression Equation (1), we calculated the Fe^{2+} contents and $\text{Fe}^{3+}/\Sigma\text{Fe}$ ratios of the garnet samples. The results are provided in Table S6, indicating that the deviation of the Fe^{2+} and $\text{Fe}^{3+}/\Sigma\text{Fe}$ ratios for most garnets samples are within 1 wt.% and 0.05, respectively, compared to the results obtained by Mössbauer (Fig. 10).

Höfer and Brey (2007)²⁵ demonstrated that for garnet samples with unknown Fe^{3+} content but known total Fe content, their L_β/L_α ratio plots below the calibration curve for $\text{Fe}^{3+}/\Sigma\text{Fe} = 0$. The magnitude of this deviation from the calibration curve (denoted as Δratio) serves as an indicator of the sample’s Fe^{3+} content. Thus, a linear equation relating $\Delta L_\beta/L_\alpha$ to Fe^{3+} content can be used to calculate the Fe^{3+} content of unknown garnet samples. The calculated $\Delta L_\beta/L_\alpha$ results are provided in Table S6. As shown in Fig. 10b, $\Delta L_\beta/L_\alpha$ exhibits a strong positive linear correlation with the Fe^{3+} content, where the latter was calculated from Mössbauer spectroscopy results and EPMA TFeO contents. We thus established a second simple linear regression equation 2, which is consistent with that reported by Cao et al. (2025)²⁸:

$$\text{Fe}^{3+} = 23.74 \times \Delta L_\beta/L_\alpha - 0.2800 \quad (R^2 = 0.9947) \quad (2)$$

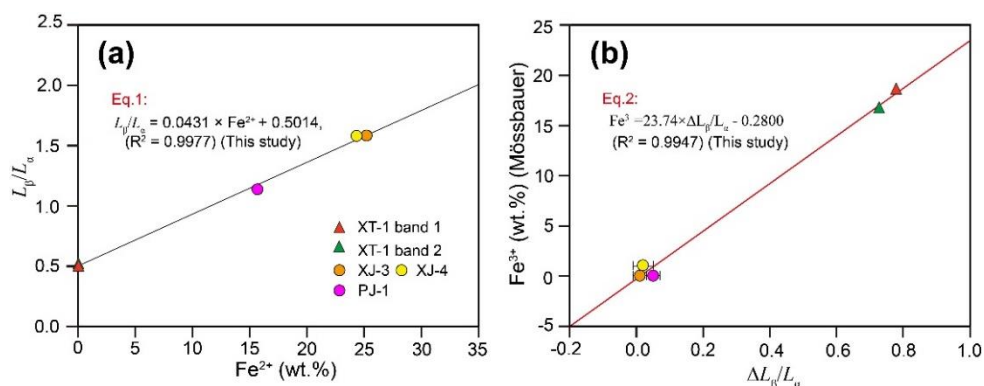


Fig. 9 Simple linear regression of Fe L_{β}/L_{α} intensity ratios (flank position ratios) against Fe^{2+} contents (a) and $\Delta L_{\beta}/L_{\alpha}$ versus Fe^{3+} contents (b) of garnet samples from this study.

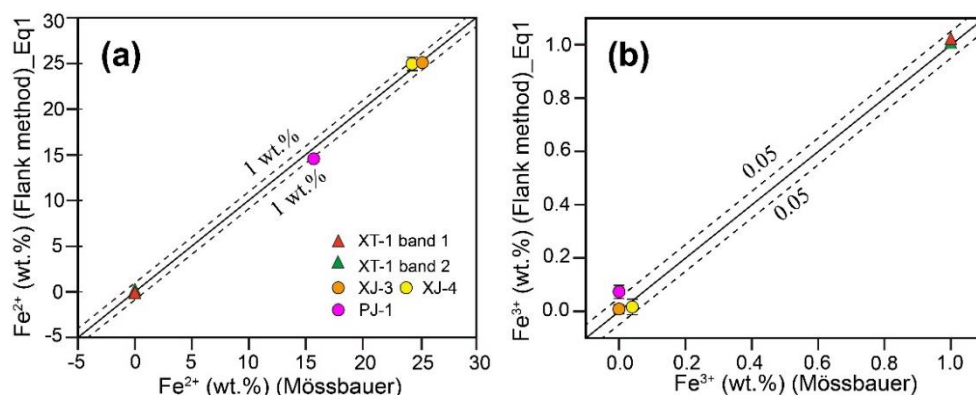


Fig. 10 Comparison of Fe^{2+} content and $\text{Fe}^{3+}/\Sigma\text{Fe}$ of garnet samples determined by the flank method using Eqn 1 and by Mössbauer spectroscopy.

The flank positions of Fe L_{α} and L_{β} determined by pure Fe^{2+} and Fe^{3+} end-number garnets are not only suitable for garnet, but in calcic amphibole, calcic pyroxene, and silicate glasses. In fact, minerals with the same crystal structure are the perfect candidate for the determination of the flank positions of Fe L_{α} and L_{β} . However, the difference spectrum obtained by minerals with the same crystal structure may show less significant than that obtained by the garnet pairs due to the variations in coordination polyhedral for Fe and the total Fe content.²¹ The flank positions determined by different pure Fe^{2+} and Fe^{3+} end-member minerals are similar.^{21,24} Therefore, pure Fe^{2+} and Fe^{3+} end-member garnets are the considerable material references to determine Fe L_{α} and L_{β} flank positions for silicate minerals enrichment in Fe. A simple linear regression equation is necessary using a series of the same group minerals with different Fe^{2+} content. However, the slope of the simple linear regression equation obtained by garnets and other minerals show significant difference.^{21-22, 24-25} This difference is attribute to the bonding environments and coordination numbers of Fe in garnet and other minerals.²⁴⁻²⁵ In addition, accelerating voltage, beam current, and beam diameter are prerequisite in minerals with different crystal structures during a long-time signal acquisition.^{22, 24} To sum up, natural pure end-member garnets are potential reference materials for the determination of Fe flank positions, and further research about standard minerals with

different crystal structures is necessary.

CONCLUSIONS

In this study, we present a series of garnet samples as natural reference materials to determine the Fe oxidation state of garnet using EPMA flank method. The conclusions of this study are as follows.

- (1) XJ-3 and PJ-1 are two pure Fe^{2+} end-member (almandine) garnets. The XT-1 is pure Fe^{3+} end-member (andradite) garnet. XJ-3, PJ-4, and XT-1 are reliable natural reference materials to define Fe L_{α} and L_{β} at flank positions.
- (2) The simple linear regressions to calibrate $\text{Fe}^{3+}/\Sigma\text{Fe}$ ratio of unknown garnets is established. The method based on this equation yields an uncertainty of ± 1 wt% for Fe^{2+} content and ± 0.05 for the $\text{Fe}^{3+}/\Sigma\text{Fe}$ ratio.
- (3) Spectrometer initialization can act as a daily calibration procedure to correct spectrometer shift for its easily exercisable and convenience.

ASSOCIATED CONTENT

The supporting information (Tables S1–S6) is available at <https://www.at-spectrosc.com>

AUTHOR INFORMATION



Di-Cheng Zhu received his BSc in 2000 from Chengdu University of Technology, and Ph.D in 2003 from Chinese Academy of Geology Sciences. He is a professor of petrology at China University of Geoscience (Beijing). His major research interests are geochemistry, petrology, and microanalysis and their applications to igneous petrogenesis,

chemical geodynamics and crustal evolution in collision zone. He has been working as co-editor-in-chief of *Lithos*, associate editor of *Geochemical Journal*, and member of editorial committee in many other academic journals. Di-Cheng Zhu is author or co-author of over 250 articles published in peer-reviewed scientific journals, with an h-index of 70 (Google Scholar). He was elected as ESI Global Highly Cited Scholar and Elsevier China Highly Cited Scholar.

Corresponding Author

* D.-C. Zhu

Email address: dchengzhu@163.com

Notes

The authors declare no competing financial interest.

ACKNOWLEDGMENTS

We thank Ren-Biao Tao for his providing garnet standard samples. We also thank Xiao-Li Li for his constructive suggestions in flank method analysis. This work was financially co-supported by the Chinese National Natural Science Foundation (42522202, 42121002, and 42330307), the Second Tibetan Plateau Scientific Expedition and Research Program (STEP) (2019QZKK0702), and the 111 project (B18048). This is China University of Geosciences (Beijing) petrogeochemical contribution PGC2015-101. XJ-3, PJ-1, and XT-1 are up to dozens to hundreds of grams. These samples were crushed to fragments and selected with no inclusion. The reported reference materials are available to scientific community by contacting the email: xuwentan1993@163.com.

REFERENCES

1. J. P. Richards, *Lithos*, 2015, **233**, 27–45. <https://doi.org/10.1016/j.lithos.2014.12.011>
2. H. W. Li, Z. M. Yang, Y. J. Lu, and Z. Q. Hou, *Nat. Commu.*, 2025, **16**, 6456. <https://doi.org/10.1038/s41467-025-61668-3>
3. J. R. Ballard, J. M. Palin, and I. H. Campbell, *Contrib. Mineral. Petrol.*, 2002, **1144**, 347–364. <https://doi.org/10.1007/s00410-002-0402-5>
4. B. A. Konecke, A. Fiege, A. C. Simon, S. Linsler, and F. Holtz, *Geochem. Cosmochim. Acta*, 2019, **265**, 242–258. <https://doi.org/10.1016/j.gca.2019.08.044>
5. M. Brounce, E. Cottrell, and K. A. Kelley, *Earth Planet. Sci. Lett.*, 2019, **528**, 115859. <https://doi.org/10.1016/j.epsl.2019.115859>
6. P. Tollan and J. Hermann, *Nat. Geosci.*, 2019, **12**, 667–671. <https://doi.org/10.1038/s41561-019-0411-x>
7. G. M. Biggar, *Contrib. Mineral. Petrol.*, 1974, **46**, 159–167. <https://doi.org/10.1007/BF00377502>
8. A. G. Tomkins, K. C. Rebryna, R. F. Weinberg, and B. F. Schaefer, *J. Petrol.*, 2012, **53**, 1537–1567. <https://doi.org/10.1093/petrology/egs025>
9. M. Tang, M. Erdman, G. Eldridge, and C. T. A. Lee, *Sci Adv.*, 2018, **4**, eaar4444. <https://doi.org/10.1126/sciadv.aar4444>
10. M. Tang, C. T. A. Lee, G. Costin, and H. E. Höfer, *Earth Planet. Sci. Lett.*, 2019, **528**, 115827. <https://doi.org/10.1016/j.epsl.2019.115827>
11. J. B. Zhang, R. Wang, and J. Hong, *Am. Mineral.*, 2022, **107**, 1779–1788. <https://doi.org/10.2138/am-2022-8141>
12. J. B. Zhang, R. Wang, F. Z. Teng, D. C. Zhu, and Z. Q. Hou, *J. Geoph. Res. Solid Earth.*, 2025, **130**, e2025JB033325. <https://doi.org/10.1029/2025JB033325>
13. M. Wilke, G. M. Partzsch, R. Bernhardt, and D. Lattard, *Chem. Geol.*, 2005, **213**, 71–87. <https://doi.org/10.1016/j.chemgeo.2005.03.004>
14. A. J. Berry, M. G. Yaxley, A. B. Woodland, and G. A. Foran, *Chem. Geol.*, 2010, **278**, 31–37. <https://doi.org/10.1016/j.chemgeo.2010.08.019>
15. E. Schingaro, M. Lacalamita, F. Scordari, and E. Mesto, *Am. Mineral.*, 2013, **98**, 709–717. <https://doi.org/10.2138/am.2013.4283>
16. P. A. V. Aken, and B. Liebscher, *Physics. Chem. Mineral.*, 2002, **29**, 188–200. <https://doi.org/10.1007/s00269-001-0222-6>
17. N. Malaspina, F. Langenhorst, P. Fumagalli, S. Tumiati, and S. Poli, *Lithos*, 2012, **146–147**, 11–17. <https://doi.org/10.1016/j.lithos.2012.04.023>
18. H. E. Höfer, G. P. Brey, B. Schulz-Dobrick, and R. Oberhänsli, *East. J. Med.*, 1994, **6**, 407–418.
19. H. E. Höfer, G. P. Brey, B. W. O. Hibberson, *Abstracts of the Tenth International Symposium on Experimental Mineral, petrol and Geochem*, 2004, **73**, 51. <https://doi.org/10.1016/j.lithos.2004.02.003>
20. S. Baier, H. E. Höfer, G. P. Brey, B. W. O. Hibberson, and A. B. Woodland, *European Mineralogical Conference*, 2012, **1**, 634. <https://meetingorganizer.copernicus.org/EMC2012/EMC2012-634.pdf>
21. Y. H. Cao, C. M. Xing, C. Y. Wang, and X. Q. Ping, *Am. Mineral.*, 2025, **110**, 1257–1268. <https://doi.org/10.2138/am-2024-9467>
22. M. Enders, D. Speer, W. V. Maresch, and C. A. Mccammon,

- Contrib. Mineral. Petrol.*, 2000, **140**, 135-147.
<https://doi.org/10.1007/s004100000179>
23. W. M. Lamb, R. Guillemette, R. K. Popp, S. J. Fritz, and G. J. Chmiel, *Am. Mineral.*, 2012, **97**, 851-961.
<https://doi.org/10.2138/am.2012.3963>
24. X. Y. Li, C. Zhang, R. R. Almeev, X. C. Zhang, X. F. Zhao, L. X. Wang, J. Koepke, and F. Holtz, *Chem. Geol.*, 2019, **509**, 152-162.
<https://doi.org/10.1016/j.chemgeo.2019.01.009>
25. H. E. Höfer and G. P. Brey, *Am. Mineral.*, 2007, **92**, 873-885.
<https://doi.org/10.2138/am.2007.2390>
26. X. L. Li, S. G. Song, L. F. Zhang, and H. E. Höfer, *Sci. Bull.*, 2018, **63**, 300-305. <https://doi.org/10.1016/j.scib.2018.01.025>
27. R. B. Tao, Y. W. Fei, E. S. Bullock, and L. F. Zhang, *Geochem. Cosmochim. Acta.*, 2018, **225**, 1-16.
<https://doi.org/10.1016/j.gca.2018.01.008>
28. Y. H. Cao, C. M. Xing, C. Y. Wang, X. Q. Ping, and X. J. Lin, *J. Anal. At. Spectrom.*, 2025, **40**, 202-215.
<https://doi.org/10.1039/D4JA00131A>
29. E. C. Hughes, B. Buse, S. L. Kearns, J. D. Blundy, G. Kilgour, H. M. Mader, R. A. Brooker, R. Balzer, R. E. Botcharnikov, D. D. Genova, R. R. Almeev, and J. M. Riker, *Am. Mineral.*, 2018, **103**, 1473-1486. <https://doi.org/10.2138/am-2018-6546CCBY>
30. C. Zhang, R. R. Almeev, E. C. Hughes, A. A. Borisov, E. P. Wolff, H. E. Höfer, R. E. Botcharnikov, and J. Koepke, *Am. Mineral.*, 2018, **103**, 1445-1454. <https://doi.org/10.2138/am-2018-6437>
31. D. C. Hezel, H. E. Höfer and A. Fichtner, *Am. Mineral.*, 2024, **109**, 1387-1393. <https://doi.org/10.2138/am-2023-9122>
32. A. J. Locock, *Comput. Geosci.*, 2008, **34**, 1769-1780.
<https://doi.org/10.1016/j.cageo.2007.12.013>
33. D. E. Groot, J. B. Thole, and G. Sawatzky, *Phys. Rev.*, 1990, **42**, 5459-5468. <https://doi.org/10.1103/physrevb.42.5459>
34. D. E. Groot. *Chem. Rev.*, 2001, **101**, 1779-1808.
<https://doi.org/10.1021/cr9900681>
-